Design Optimization of an Additively Manufactured Prototype Recuperator for Supercritical CO_2 Power Cycles

Ed Robey[1,3], Sridharan Ramesh[1,3*], Adrian S. Sabau[4], Abas Abdoli[5], James Black[2], Doug Straub[1], and Joe Yip[1]

[1]*National Energy Technology Laboratory, 3610 Collins Ferry Road, Morgantown, WV 26507, USA*
[2]*National Energy Technology Laboratory, 626 Cochrans Mill Road, P.O. Box 10940, Pittsburgh, PA 15236-0940, USA*
[3]*NETL Support Contractor, 3610 Collins Ferry Road, Morgantown, WV 26507, USA*
[4]Computational Sciences & Engineering Division, *Oak Ridge National Laboratory, 1 Bethel Valley Rd, Oak Ridge, TN 37831*
[5]*TKelvin, 1545 Wigwam Parkway, Henderson, NV 89074*
**Email: sridharan.ramesh@netl.doe.gov*

ABSTRACT

Supercritical CO_2 (sCO_2) power cycles are being developed due to their potential for high efficiency and reduced capital cost. It is necessary that these recuperators operate at high pressures and temperatures, up to 30 MPa and 900 K, with effectiveness values >95% and pressure drops <1% to achieve high cycle efficiencies. Moreover, it is also necessary to have reasonable cost recuperators to control the capital costs of the sCO_2 power cycles. In this study, a Plate Pin-Fin (PPF) heat exchanger has been proposed as an sCO_2 recuperator. This preliminary recuperator design leverages capabilities enabled by additive manufacturing. Although the PPF design has characteristics similar to those of a plate heat exchanger, small diameter and relatively long fins are used to increase surface area, enhance heat transfer, and provide structural support for the partition plates that separate the fluid streams. Existing correlations for heat transfer and pressure drop were adapted for the PPF heat exchanger. These correlations were implemented in a 1D analytical model and used for the optimization of a 5-kW_{th} high temperature recuperator for an indirect sCO_2 cycle by varying the design parameters to minimize the quantity of material required. A 3D conjugate heat transfer numerical simulations were conducted to validate the heat transfer and pressure loss correlations. A steepest descent method was used to minimize heat exchanger mass for a 5-kW prototype recuperator subject to a maximum specified pressure drop. The design analysis indicated that an optimum PPF recuperator would be attained for the minimum allowable pin transverse spacing, minimum pin width, minimum pin height and near maximum cell aspect ratio. At a low material requirement of 0.216 kg/kW and a pressure drop, which is almost five times lower than the allowable pressure drop design target, the optimized PPF heat exchanger has the high potential to be an alternative to a printed circuit heat exchanger, which is a conservative design basis for the current state-of-the-art sCO_2 recuperators.

***Notice**: This manuscript has been authored in part by UT-Battelle, LLC, under contract DE-AC05-00OR22725 with the U.S. Department of Energy (DOE). The United States Government retains and the publisher, by accepting the article for publication, acknowledges that the United States Government retains a non-exclusive, paid-up, irrevocable, world-wide license to publish or reproduce the published form of this manuscript, or allow others to do so, for United States Government purposes. The DOE will provide public access to these results of federally sponsored research in accordance with the DOE Public Access Plan (http://energy.gov/downloads/doe-public-access-plan).*

1.0 INTRODUCTION

Supercritical carbon dioxide (sCO_2) is receiving attention as a working fluid for power generation because of its potential for high efficiency and power density [1–3]. The indirect sCO_2 recompression closed Brayton cycle (RCBC) is gaining interest as a more efficient alternative to steam Rankine cycles for nuclear, coal, gas, and concentrated solar power plants [4]. A 10 MWe sCO_2 pilot plant is being constructed in San Antonio, Texas with support from the U.S. Department of Energy. This Supercritical Transformational Electric Power (STEP) project will demonstrate a simple closed recuperated cycle configuration initially operating at 500 °C turbine inlet temperature. After commissioning the simple cycle configuration, the RCBC configuration will be demonstrated with a turbine inlet temperature of at least 700 °C [4–6]. An important characteristic of sCO_2 power cycles is the need for high levels of heat recuperation to achieve the high efficiency potential.

Heat recuperation is of crucial importance for the economics and performance of sCO_2 Brayton power cycles. Dyreby et al. [7] and Zitney et al. [8] showed the importance of heat transfer from the hot turbine outlet stream to the cold compressed inlet stream, and the subsequent effects on the overall efficiency, performance, and dynamic behavior of an sCO_2 Brayton cycle. As part of the STEP program [4–6], Zitney et al. [8] modeled and demonstrated the steady state, dynamic, load-following, startup and shutdown operations involved in an sCO_2 Recompression Brayton power cycle. A shell-and-tube type heat exchanger was modeled for the primary heater, recuperators, and coolers in a counterflow arrangement. The design approach temperature for the recuperator was set to 10 K. At steady-state operating conditions, the net heat transferred from both the high temperature (45 MW_{th}) and the low temperature recuperator (14.4 MW_{th}) was roughly 2.8 times the net heat input (21.3 MW_{th}) to the cycle. In an optimally designed sCO_2 Brayton cycle, the heat duty in the recuperators is expected to be much larger than the net power output [8, 9].

Jiang et al.[10] presented a model developed in Aspen to design and optimize the micro shell-and-tube type heat exchanger for high and low temperature recuperators to be used in the 10 MWe STEP plant [4–6]. For the same application, a printed circuit heat exchanger (PCHE) was designed and modeled as a baseline for the high and low temperature recuperators of the sCO_2 power cycles [11]. To reduce sCO_2 capital cost and plant size, specially designed compact heat exchangers are desired as a better option than conventional shell-and-tube heat exchangers (CSTEs). Furthermore, a comparison among the PCHE, micro shell-and-tube heat exchanger (MSTE), and CSTE indicated that the PCHE is the best candidate for recuperators used in the 10 MWe sCO_2 Brayton cycle because of its compactness, fast dynamic response, and mature state of the manufacturing processes. Kruizenga [12] indicated that PCHEs were considered as the state-of-the-art heat exchangers for sCO_2 power cycles due to their large surface area available for heat transfer. Although PCHE is a mature technology, PCHEs employ heavy metal sections, with a relatively small flow area per unit volume. Le Pierres et al. [13] discussed the common misconceptions on performances of PCHE concepts used in the literature while addressing the mechanical considerations and challenges involved in the design process. Also, the folded-wavy-fin and wire-mesh HX were not considered for baseline due to long term operational concerns (Sabau et al. [14], & Kung et al. [15]) of oxide scale growth in these HXs that employ both convex (outside) surfaces and the concave (inside) surfaces. Therefore, the effective selection, design, and operation of such recuperators are crucial for the successful demonstration and commercialization of sCO_2 Brayton cycles.

Thus, one of main objectives of this study is to explore the recuperator design space for sCO_2 power cycles. The approach taken in the current study is slightly different from conventional heat exchanger studies in the literature. Studies focusing on heat exchanger designs rely on improvements to heat transfer capability, reductions in pumping power or a combination of both (thermal performance factor) [16]. Most of the time, these conceptual designs have not been fabricated. In the our study, the designing a novel 5 kW prototype recuperator was considered with the aim of fabricating it for subsequent testing in NETL's Heat Exchange and Experimental Test (HEET) facility [17]. Successful testing and validation of critical performance metrics with other state-of-the-art heat exchangers, which were considered for the 10 MWe STEP power plant, will pave the way for future HX designs. To allow flexibility in fabrication, additive manufacturing (AM) was considered for this first study. Musgrove et al. [18] discussed the potential of additive manufacturing in designing and developing heat exchangers to reduce the cost while still delivering better performance than the current state-of-the-art technologies. Sabau et al. [19] explored additive manufacturing as a route to advance the performance of heat exchangers. Certain intricate features designed to enhance heat transfer may be too complex for standard manufacturing but could be possible via additive manufacturing (AM). The fabrication scale-up, including an assessment of AM applicability, needs to be conducted for the most promising geometries identified in this study. Being free to consider other geometries than those currently enabled by current fabrication techniques, this study seeks potential cost reductions in manufacturing a sCO_2 recuperator while still delivering a similar thermal performance.

In this study, a Plate Pin Fin heat exchanger (PPF HX) concept is proposed for RCBC recuperator applications due to the possibility of high effectiveness. This concept was developed based on a careful consideration of all the heat exchangers for RCBC that were reviewed in this section. The PPF design has characteristics similar to those of a plate heat exchanger with small diameter to increase surface area, enhance heat transfer, and provide structural support for the partition plates that separate the hot and cold fluid streams. This preliminary recuperator design takes advantage of several capabilities enabled by additive manufacturing while considering features that can be scaled up. In this study, geometric variations of the PPF design are examined analytically via a 1D steady-state model to identify designs with performance comparable to more standard designs such as printed-circuit heat exchangers. The 1D heat exchanger model utilized a goal-seek function to vary the number of cells until a heat transfer rate of approximately 5 kW was reached. The heat transfer and pressure loss predictions from this 1D model are then verified through computational fluid dynamics simulations.

Nomenclature

a	Elliptical Cell major radius
A_{plate}	Area of elliptical plate
b	Elliptical Cell minor radius
Cp	Specific heat capacity
C_R	Ratio of minimum and maximum Cp's
D_{eq}	Equivalent Diameter of the Elliptical Plate or Cell
d_{pin}	Hydraulic diameter of a pin fin
h	Heat transfer coefficient
H_{pin}	Pin length
k	Thermal conductivity
L_{avg}	Pin fin size factor
L_{maj}	Length of the major axis of the pin fin
L_{min}	Length of the minor axis of the pin fin
L_{wall}	Wall thickness (solid plate and outer shell)
N	Number of flow cells in the PPF HX
Q	Heat transfer rate
RANS	Reynolds Averaged Navier-Stokes
S_L	Longitudinal pin spacing
S_T	Transverse pin spacing
T_g	Mean centerline fluid temperature upstream of a pin fin
T_w	Area averaged pin fin wall temperature
V_{in}	Channel inlet velocity for the CFD model
Y_f	Dimension of pin-free zones
γ_e	Aspect ratio of the elliptical plate or cell, a/b
γ_{pin}, γ_p	Pin fin shape factor
μ	Dynamic viscosity
ρ	Density

Subscripts

cold	Cold side of the recuperator
c, in	Inlet conditions on the cold side of the recuperator
cond	Condition
hot	Hot side of the recuperator
Primary.pop	Primary Population

2.0 METHODS

A description of the PPF HX design features and geometry are described in this section. In addition, the optimization and Computational Fluid Dynamics (CFD) approach to validate the 1D analytical model will also be described in this section. A detailed description of the heat transfer and pressure loss correlations used in this model is provided in Appendix I. Based on the sizes of geometrical features, the Laser Powder Bed Fusion Additive Manufacturing (LPBFAM) was selected as a viable method for fabrication [18]. Thus, the smallest size of geometrical features is limited to those of the LPBFAM process.

2.1 PPF GEOMETRY

The base unit of the PPF heat exchanger consists of an elliptical flow cell. A flow cell consists of the flow passage, pin fins and the two end walls of the plate separating the hot and cold fluid. Fluid is distributed near the major axis at one end of the ellipse and flows across a pin field in the center prior to exiting the cell through a manifold near the opposite end. The ellipse has an area of $\pi\, {D_{eq}}^2/4$ and an aspect ratio of $\gamma_e = \frac{a}{b}$ where 'a' and 'b' are the major and minor radii of the ellipse (Figure 1). The depth of the elliptical cavity is determined by the pin length, H_{pin}. There are pin-free areas near the inlet and outlet of each cell. The size of these pin-free zones, along the major axis, is specified by the ratio $\left(\frac{Y_f}{a}\right)$. Although the designer may place pins in these "pin-free" zones for flow distribution and/or structural considerations, those pins are not included in the 1-D heat transfer model.

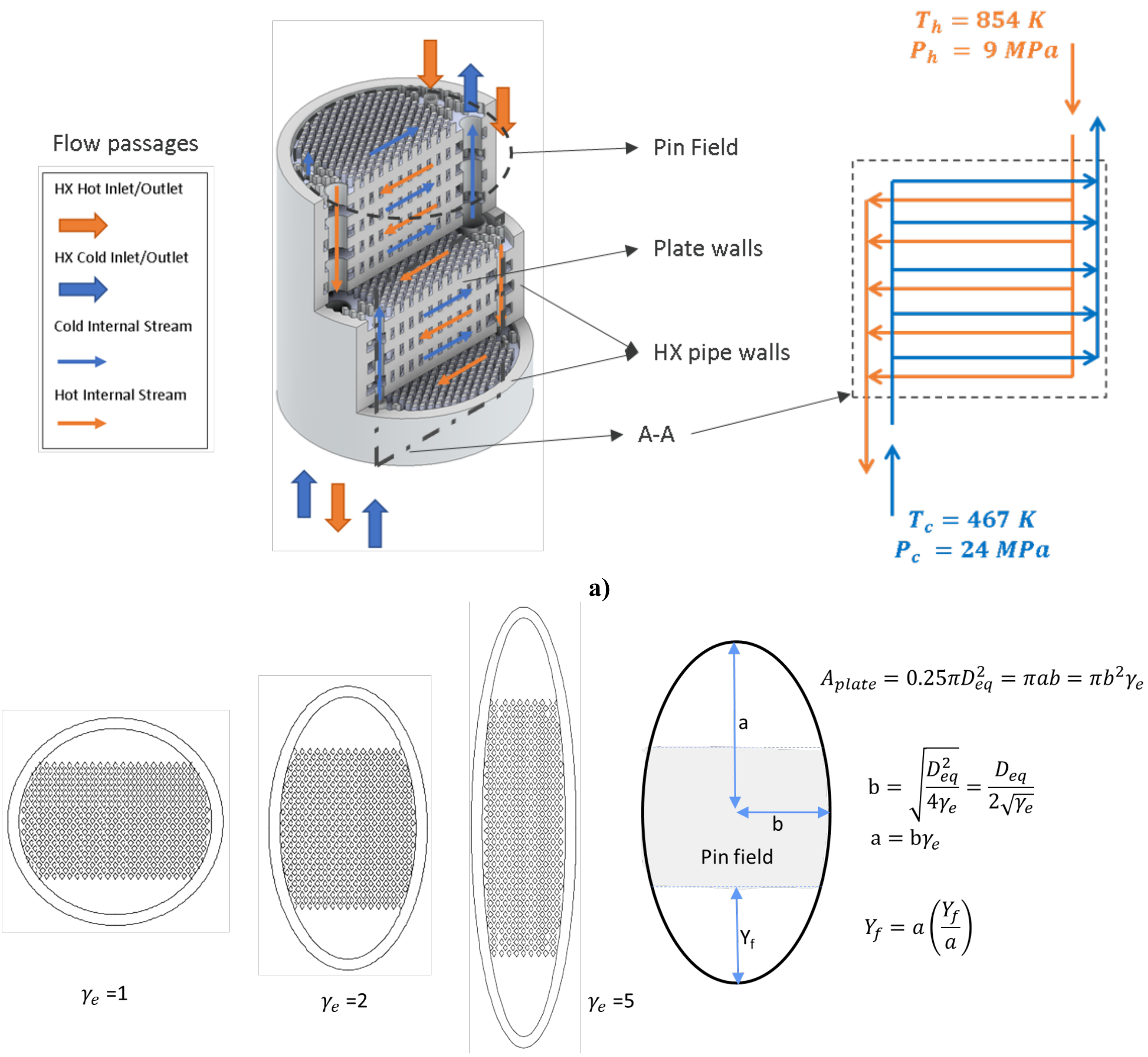

a)

b)

FIGURE 1. a) Section view of plate fin heat exchanger for sCO2 recuperator along with sample flow network, b) Geometric parameters for the PPF elliptical plates.

The pin fins are diamond-shaped in cross-section (Figure 2). The size of the pin fin in cross-section is controlled by $L_{avg} = \sqrt{L_{maj} \cdot L_{min}}$, where L_{maj} is the major axis length of the pin fin (parallel to the major axis of the ellipse) and L_{min} is the minor axis length of the pin fin. The parameter $\gamma_{pin} = \frac{L_{maj}}{L_{min}}$ controls the pin “shape”. The transverse pin spacing is S_T. The lateral pin spacing is determined from the (S_L/S_T) ratio. The pin density is $\frac{1}{S_T^2\left(S_L/S_T\right)}$.

The total number of pins per cell is the product of pin density and the area of the semi-elliptical pin field. This area is calculated by subtracting the pin free area at both ends from the total area of the ellipse. The pin free area is calculated via numerical integration. The heat exchanger consists of an even number of these elliptical cells, arranged in an elliptical prism-shaped stack. Half of the cells contain the hot fluid and are inter-leaved with the other half containing the cold fluid. The hot and cold fluids pass through their respective cells in opposite directions, making the PPF heat exchanger counter-flow in nature.

Heat exchange occurs from the fluid in the hot cells to that in the cold cells via convection to the primary surfaces (cell walls or “plates”) and secondary (pin) surfaces, with conduction across the cell walls. The cell perimeter walls and the two elliptical plates at the ends of the stack are assumed to be adiabatic. In this implementation of the model, only the primary and secondary surfaces in the pin field are considered. The surfaces in the pin-free zones are ignored.

Each cell exchanges heat with its two neighboring cells, except for one cold and one hot cell located at either end of the stack. These two cells have only one neighbor. Although the pins span the cavity within each cell, pins in the cells that have two neighbors are modeled as two half-length pins that meet in the middle. For the two end cells that exchange heat with only one neighbor, the pins are modelled at their full pin length. The distinction between half-length and full-length pins affects the pin efficiency calculations. Additional details relative to the geometry and calculation of heat exchanger in the 1D PPF model are included in the Appendix I. References for the heat transfer and pressure drop correlations used in the 1D PPF model can be found in [20–23].

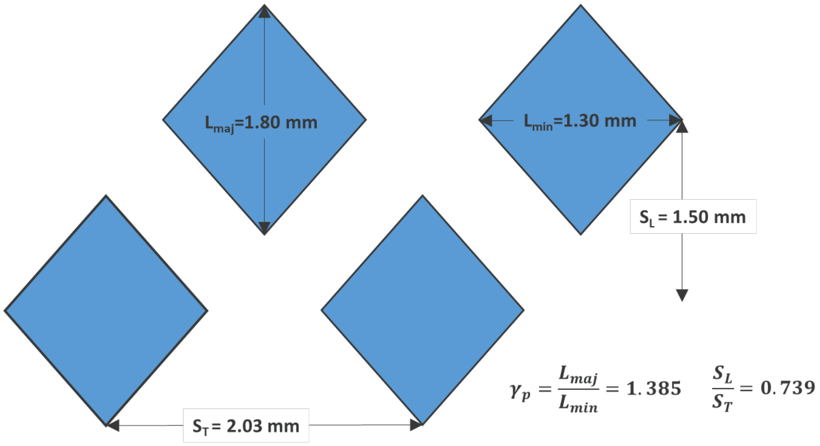

FIGURE 2. Example of PPF pin fin geometry.

2.2 OPTIMIZATION CRITERIA

A PPF heat exchanger design can be found to approximate any specific heat duty by varying the geometric parameters and number of cells. Whether or not such designs would be practical from the perspectives of material expense, physical size, pressure loss, and manufacturing considerations remains to be seen. The PPF model is used to identify 5kW designs that are manufacturable and compatible with other heat exchanger designs with respect to the specific mass and pressure loss characteristics. The objective of minimizing the mass is based on the assumption that the heat exchanger mass will be an important factor in the overall cost of an additively manufactured component.

2.3 HEAT ENHANCEMENTS IN PPF DESIGN AND MODEL VALIDATION

One of the objectives of the current study is to develop a reduced order heat transfer model as a simple yet viable approach to design a plate pin fin heat exchanger. As shown in Appendix I, heat transfer and pressure drop correlations are used for the purposes of evaluating the thermal characteristics of the PPF HX. The accuracy of results largely depends on the applicability of the correlations. In this section, the heat transfer coefficient on a pin fin surface, which accounts for roughly 75% of the heat exchanger area and deemed critical is validated with the help of numerical predictions. The role of 3D CFD simulation is limited to the comparison of the empirical correlation developed for a bank of tubes to the pin fin banks present in the PPF HX. It is not used to design the heat exchanger as such. It must be noted that the heat transfer coefficient on the end walls were estimated separately in the 1D model (see Appendix I).

Preliminary results using the 1D heat exchanger model showed that a PPF HX designed for 5 KW would require multiple flow cells (> 6) each containing at least 300 pin fins. Owing to the large number of pin fins predicted per cell, the computational cost associated with the simulation of even a single flow cell would be too high. Thus, a considerably shorter domain needs to be modeled to reduce the run time of the numerical simulations. As explained in [24], the convection heat transfer coefficient increases with increasing pin fin row number until approximately the 5th row after which there is marginal change in turbulence and heat transfer. In the current study, 36 rows of pin fins are modeled as shown in Figure 3, to be on the conservative side.

Steady state Reynolds-averaged Navier–Stokes (RANS) equations were solved with Realizable k-ε and enhanced wall treatment model providing closure for turbulence and near wall modelling. Most commonly used turbulence models for predicting internal flow and pin fin heat transfer are Realizable k-ε and SST k-ω model. A study by Weihong Li [25] assessing the performance of various turbulence models for narrow passages created by pin fin arrays recommended Realizable k-ε model for predicting pin fin surface Nusselt number distribution. Momentum, energy and turbulence equations were discretized using a second order scheme. A coupled solver in conjunction with a pseudo transient method was found to provide smoother and faster convergence when compared to using pressure-velocity coupled algorithms such as SIMPLE. The convergence criteria were set to 1E-6 for all the equations.

The thermophysical properties were evaluated at a mean temperature and pressure (642.7352 K & 24 MPa) for the cold fluid as estimated by the 1D model. In general, the high temperature recuperators of an indirect sCO_2 power cycle are operated further away from the critical point and pseudo-critical line. Unlike the actual PPF HX, the numerical domain is considerably shorter. The centerline fluid temperature was found to change by roughly 32.7 K from inlet to outlet which spans 36 rows of pin fins. A 30 K increase in bulk temperature on the cold side causes ~-0.38%, 2.26%, 3.77%, & -5.53% respective change in the thermophysical properties: Cp, μ, k, & ρ. This is expected to change the Nusselt number and heat transfer coefficient by ~ -2.5% and 1.18% respectively. Hence, constant thermophysical were found to be sufficient for the purposes of this numerical study.

A grid sensitivity study was conducted using a shorter domain consisting of nine rows of pin fins instead of 36. It was observed that a reduction in the mesh element size from 0.1 mm to 0.05 mm caused less than 0.7% change in both the pressure drop and the average heat transfer coefficient on the pin fin surface. To be more conservative, a final cell size of 0.025 mm was selected. This resulted in roughly 12.76 million tetrahedral elements for the original numerical domain with 36 rows of pin fins. The first layer element size was selected such that the wall y^+ would be close to 1. Figure 4 shows the mesh at select locations (L_1, L_2, & L_3; refer Fig. 3).

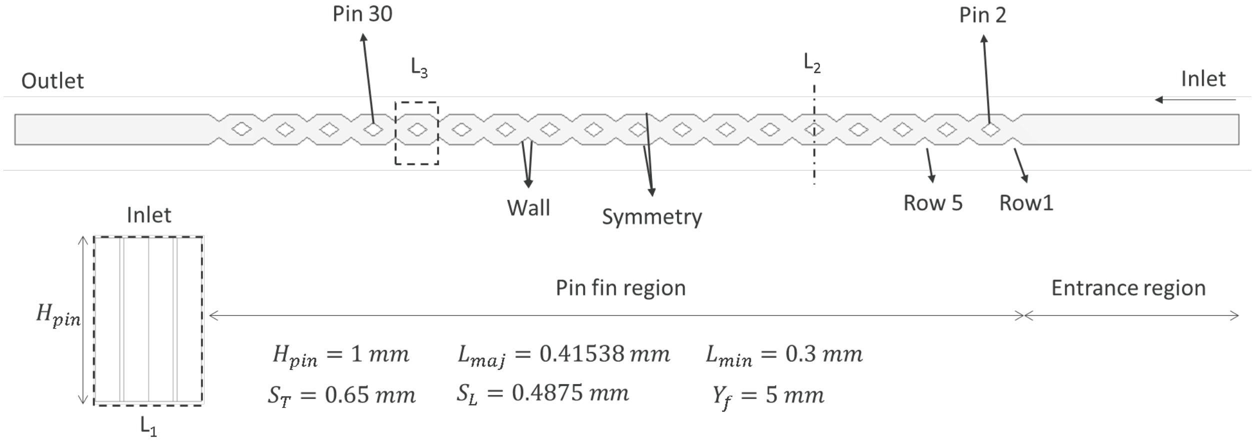

Figure 3. Numerical domain

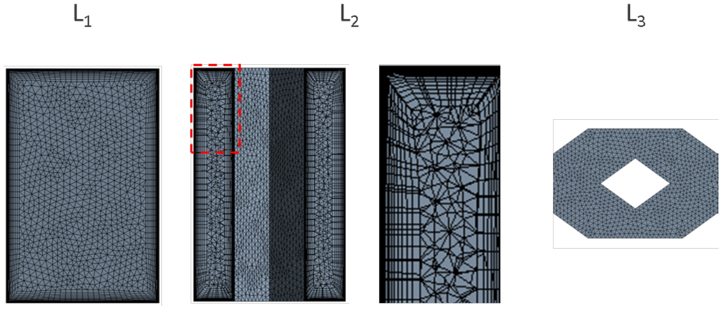

Figure 4. Tetrahedral mesh at different locations along with the inflation layers near the wall

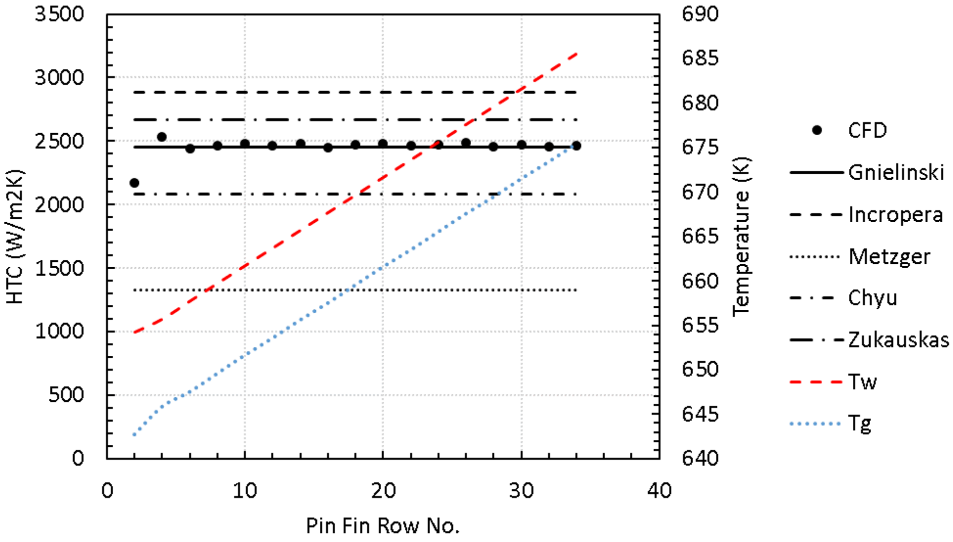

Figure 5. Comparison of numerical predictions and analytical correlations for heat transfer coefficient

A uniform velocity ($V_{in} = 0.16131\ m/s$) boundary condition was provided at the inlet such that it would match the heat exchanger model's flow cell velocity and the Reynolds number estimated using pin fin's hydraulic diameter ($d_{pin} = 0.243\ mm$). A symmetry boundary was used wherever applicable. The domain outlet was provided a constant pressure outlet boundary condition. The 1D heat exchanger model relies on a correlation developed for a bank of tubes (Eq. 20-23) to estimate the heat transfer coefficient on the pin fin surfaces. Due to the turbulence generated by the pins, the choice of boundary condition on the pin fin surface is expected to have limited influence on the heat transfer coefficient. In the current study, a constant heat flux boundary condition was used on the pin fin surfaces. The end walls on either side (top and bottom) of the flow cell were treated as adiabatic walls as they are expected to have little influence ($H_{pin}/d_{pin} > 4$).

The heat transfer coefficient was then estimated using the channel centerline temperature just upstream of a pin fin and the area averaged pin fin surface temperature along with the known wall heat flux. Figure 5 shows the predicted wall & fluid temperature, and the predicted heat transfer coefficient along the pin fin rows. Several empirical correlations [26–30] developed for either a bank of tubes or pin fin arrays were also analyzed to evaluate their applicability for the 1D heat exchanger model. The predicted heat transfer coefficient was found to match Gnielinski's correlation [26] closely.

The 1D heat exchanger model follows Gnielinski's correlation [26] to estimate the pin fin heat transfer coefficient. It must be noted that the characteristic Reynolds number (Eq. 19) used to estimate the pin fin Nusselt number had to be adapted to be consistent with the development of a reduced order PPF heat exchanger model.

3.0 RESULTS AND DISCUSSION

3.1 MODEL SOLUTION

Given the process mass flow rates, inlet temperatures, inlet pressures (Table 1, [31]), and other geometric parameters, the 1D heat exchanger model calculates the number of cells (N) required to achieve the target heat duty Q (Q(N) ≅ 5 kW), in addition to the pressure drop and mass of the solid volumes. The pressure and temperature conditions were chosen to represent a high-temperature recuperator in a process flow diagram of a sCO$_2$ cycle [32]. The mass flow rates of the hot and cold streams were scaled down in proportion to the heat removed. In the current study, the performance of a scaled-down heat exchanger of a size appropriate for fabrication through AM and testing at NETL's HEET rig target capacity of 5 kW$_{th}$ was chosen. Since the inlet conditions and mass flow rates for both streams are constant, a constant heat duty also results in the same outlet temperatures and approach temperatures for all cases. The effectiveness for the 5 kW model results described in this paper is 97%.

Table 1. Operating conditions and boundary conditions for the 1-D heat exchanger model

Fluid	Inlet Temperature (K)	Inlet Pressure (MPa)	Mass Flow Rate (kg/sec)

Hot Fluid	CO_2	854	9	0.0114
Cold Fluid	CO_2	467	24	0.0114

The mass of metal and the pressure loss across the heat exchanger are recorded along with the heat exchanger geometry for subsequent analysis. As the total heat transferred is a function of the number of cells, an understanding of that relationship is critical to understanding other results.

3.2 BASELINE 5 kW PPF HX CONFIGURATION

As a starting point, the baseline HX with circular shaped plates was selected ($D_{eq} = 57.2\ \mathrm{mm}, \gamma_e = 1$). A common staggered arrangement of the pin fins was selected ($S_T = 2.03\ \mathrm{mm}, \& \frac{S_L}{S_T} = 75\%$, as shown in Figure 2). Under the baseline set of geometric parameters ($\frac{\gamma_f}{a} = 55.7\%, L_{wall} = 3\ \mathrm{mm}, H = 3\ \mathrm{mm}, L_{avg} = 1.53\ \mathrm{mm}, \gamma_p = 1.385$) a PPF with only two cells is estimated to transfer 866 W or 17% of the 5 kW target (Figure 6). Doubling the number of cells doubles the heat transfer surface area but also decreases the mass flux per cell by a factor of two, the net result of which is in an increase in Q to 31% of the 5-kW target. Each additional pair of cells results in a smaller increase in Q. A total of 100 cells is required to achieve 4 kW, but it requires an additional 2,286 cells to achieve 5 kW. The mass of metal required for fabrication of the heat exchanger increases roughly linearly with the number of cells. The pressure loss decreases with an increasing number of cells.

The total number of cells was not constrained to even integers or to integers. Hence most model results except when otherwise noted include a non-integer number of cells. It was felt that these results would still illustrate the model performance and that the distinction between 2,386 cells and 2,386.75 cells is trivial.

3.3 OPTIMIZATION OF 5 kW PPF HX

In this section, we analyze the (PPF) 1D heat transfer model to help identify those 5kW designs that are manufacturable and compatible with other heat exchanger designs with respect to the specific mass and pressure loss characteristics. This goal is approached from two directions. First, the parameters will be examined analytically using the underlying equations and then a factorial design of experiments method will be used to exercise the model and analyze the resulting designs. Finally, an optimization that uses a "steepest-descent" approach will also be used to minimize the PPF HX mass.

3.3.1 Discussion of independent geometric parameters and expected impact on PPF performance

The total number of PPF cells required to achieve 5 kW_{th} (and the mass of the resulting heat exchanger) is likely to be low when the thermal resistance is low. The total thermal resistance will be low when the products of the heat exchange coefficients and the heat exchange areas are high. Many of the PPF geometrical parameters impact the thermal resistance in predictable manners. The effects of the various geometric parameters in the PPF model are examined analytically in this section to identify optimal settings and to better understand how they interact in the model.

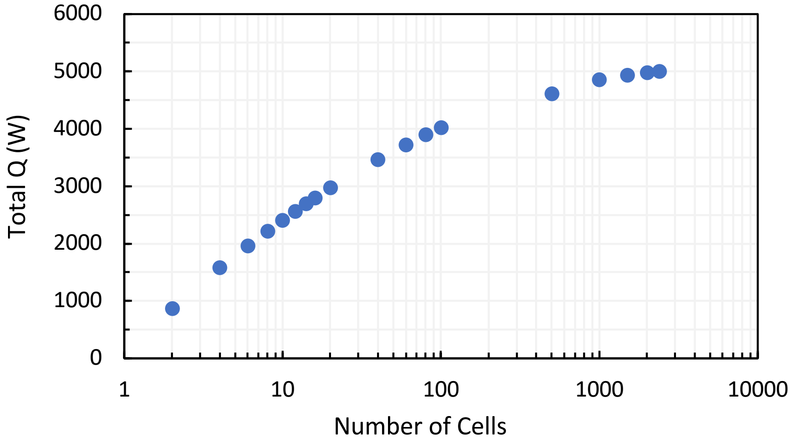

FIGURE 6. No. cells or plates required vs. HX heat capacity for the baseline PPF configuration.

Pin Size and Shape (L_{avg} and γ_{pin}): The size and shape of the pin fins are regulated by L_{avg} and γ_{pin}. Heat exchanger material volume is used as a surrogate for mass. The pin surface area per unit volume is calculated as shown in Equations 1-3. The pin surface area is the product of the pin perimeter and the pin length:

$$A_{pin} = 2H_{pin}L_{avg}\sqrt{\gamma_{pin} + {}^{1}/_{\gamma_{pin}}} \tag{1}$$

The volume of a pin is

$$V_{pin} = \frac{H_{pin}}{2}L_{avg}^{2} \tag{2}$$

and the pin heat exchanger surface to volume ratio becomes

$$\frac{A_{pin}}{V_{pin}} = \frac{4\sqrt{\gamma_{pin}+{}^{1}/_{\gamma_{pin}}}}{L_{avg}} \tag{3}$$

Therefore, the surface area to volume ratio is maximized by small pins and/or pins that have high aspect ratio and narrow in cross section. This is useful information in that it suggests that the heat exchanger mass will be reduced by decreasing L_{avg} and increasing γ_{pin}. However, it is obvious that minimum feature size limits for the LPBFAM process will be encountered. Two minimum pin dimensions are considered in the factorial design of experiments study (i.e., L_{avg} dimensions of 0.25 and 0.35 mm). With diamond shaped pins this small, potential solutions that increase the pin aspect ratio may not be feasible since the very thin points on these diamond shaped pins may not be accurately fabricated.

Pin Length or Pin Height (H_{pin}): Increases in pin length increase the pin surface area without changing the pin area-to-volume ratio. From this perspective, longer pins would be better. However, the cell "depth" also increases with longer pins, thereby decreasing the mass flux (and the heat transfer coefficient). The pin efficiency also decreases as the pin length increases. For these reasons, it would be reasonable to expect that these counter-acting effects will lead to an "optimum" pin length for fixed values of other geometric variations.

The pin length also comes into play in the trade-off between the primary and secondary heat transfer areas. Each pin added to a cell removes the primary heat transfer area on both ends. If the length of a pin $H_{pin} > \left(\frac{h_{primary}}{h_{pin}\epsilon_{pin}}\right)\frac{0.5}{\sqrt{\gamma_{pin}+{}^{1}/_{\gamma_{pin}}}}L_{avg}$, then the pin adds more secondary heat transfer than is lost to primary heat transfer. For the baseline geometry, the length required to satisfy this criterion is 0.02 mm. Hence any practical length pin would be worth including in the analysis.

Pin Spacing ($S_T - L_{min}$ and/or S_L/S_T): Decreasing S_T and/or the S_L/S_T ratio will increase the pin heat exchange area by increasing the number of pins without any changes in the pin area-to-volume ratio. Additional benefits are induced by increases in mass flux (and the heat transfer coefficient). Benefits of decreasing both these parameters will be seen until a limit is reached when the "gaps"' between adjacent pins become too small for the LPBFAM process. It is assumed that this limit will be reached when the pin-to-pin gap reaches 0.25 or 0.35 mm. Without this restriction, it is expected that any optimization procedure would minimize the inter-pin gap until $S_T/(S_T-D_{pin})$ approaches infinity.

Free board (Y_f/a): By decreasing the "free" space at either end of the flow cell, more pins will be added with the associated increase in pin mass but no change in the pin surface to volume ratio. As a certain amount of space will be needed for the inlet and outlet flow connections, we have arbitrarily restricted Y_f/a to a minimum of 0.25.

Plate Size (D_{eq}): Increasing the equivalent cell diameter increases the primary and secondary heat exchange area per cell while minimizing the ratio of the heat exchange area to cell mass. However, increasing the D_{eq} also increases the average cross-sectional area, which decreases mass flux and the heat transfer coefficient and can increase the number of cells. In the PPF, minimizing mass could drive D_{eq} towards the upper limit of the LPBFAM technology.

Plate Aspect Ratio (γ_e): Changing the plate aspect ratio does not affect the heat exchange area but it makes the flow cell narrower, thereby reducing the average cross-sectional area and increasing the mass flux and heat transfer coefficient. A slight negative effect is seen in increases of perimeter mass relative to the heat exchange surface area. The impact of these counteracting effects in determining an optimum aspect ratio needs to be explored. A trend toward long narrow channels and large cell diameters could be too large and/or too long for some commercial LPBFAM, or other, fabrication techniques.

Perimeter thickness and plate wall thickness (L_{wall}): Both contribute directly to cell mass without any significant impact on heat exchange. The plate wall thickness does play a role in the conductance resistance, but the role is minor when combined with convective resistances. Procedures to minimize heat exchanger mass will decrease these thicknesses until they reach limits imposed by structural considerations. This parameter will be treated as a constant in the following analysis.

3.3.2 Full Factorial Design

A full factorial experiment was conducted on the PPF model geometric parameters listed in Table 2. A range of equivalent diameters (with respect to the baseline equivalent diameter, D_0) and ellipse aspect ratios, γ_e, was chosen to help elucidate the location of geometric optimum with respect to the heat exchanger mass. Three pin lengths (1, 2, and 3 mm) were chosen keeping in mind the feasibility of the design from the LPBFAM perspective and that was also likely to enclose the optimum. The discussion from the previous section has already confirmed that the absolute optimum values of pin size and pin spacing would be too small to be considered practical for the LPBFAM process, so both of these parameters were initially set at a constant 0.24 mm. After some further consideration, it was thought that $L_{avg} = 0.24$ mm may in fact be too small also, so another set of model run was made with $L_{avg} = 0.35$ mm.

Table 2. PPF Geometric Parameters for the full factorial experiment

Parameter	**Values**						
D_{eq}/D_0	0.5	1.0	1.5	2.0	2.5	5.0	7.5
γ_e	1.0	1.5	2	2.5	3	4	5
H_{pin} [mm]	1	2	3				
L_{avg} & (S_T-L_{avg}/γ_{pin}) [mm]	0.24	0.35					

The free-space parameter was set to $Y_f/a = 0.25$. The thickness of the plates that separate the flow cells, and the thickness of the perimeter walls that enclose the flow cells were both set to a "reasonable" minimum of 0.6 mm. Results for $L_{avg} = 0.35$ mm are shown in Figure 7. It is important to recall that each data point in Figure 7 represents a unique geometry with identical hot and cold fluid temperatures, pressures, flow rates, and rate of heat transfer from the hot to the cold fluid. It is also important to realize that the number of cells needed for a geometry to transfer a heat rate of 5 kW is usually not an integer. The results, whether an even integer number of cells or not, still demonstrate the important trends and the geometric combinations that yield less massive heat exchangers. It must be noted that the structural aspects have been considered while selecting the range of values for each design parameter. Pin-fins also have a structural supporting role. Prior experience with designing and building a dedicated test facility to study supercritical CO_2 at extremely high pressures [17,33] was leveraged in this study. Additionally, additive manufacturing constraints were taken into the design consideration.

The heat exchanger mass decreased with increasing plate diameter up to a D_{eq}/D_0 ratio of 2 to 3, after which the total mass began to increase. This optimum of 2-3 times the baseline PPF diameter seems consistent across the other parameters. Over an a/b range of 1-5, the PPF heat exchanger mass continued to decrease, but with decreasing returns. Of the three pin lengths studied, the 1 mm pin length yielded the least massive PPF heat exchangers. Based on these trends, an optimum design for a 5 kW recuperator would have an equivalent diameter of ~2.5 times the baseline PPF, with an aspect ratio of 5 and a total core mass of ~1 kg. The results for the runs with a pin size of 0.24 mm were similar with respect to the trends. The optimum heat exchanger mass, however, was less due to the higher area to mass ratio of the smaller pins.

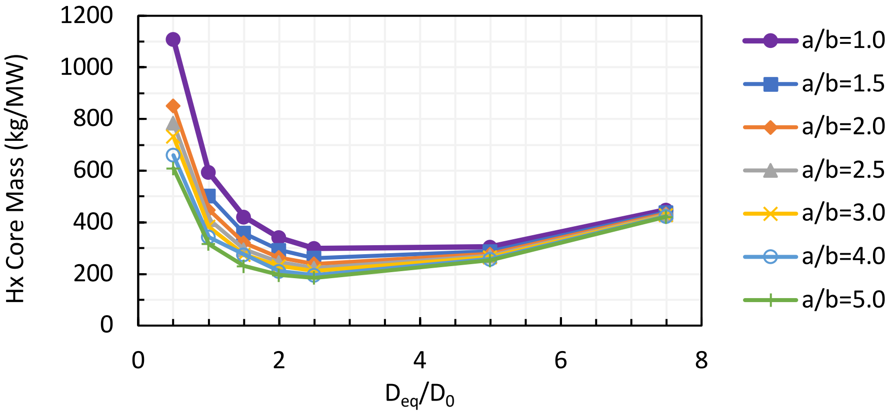

a)

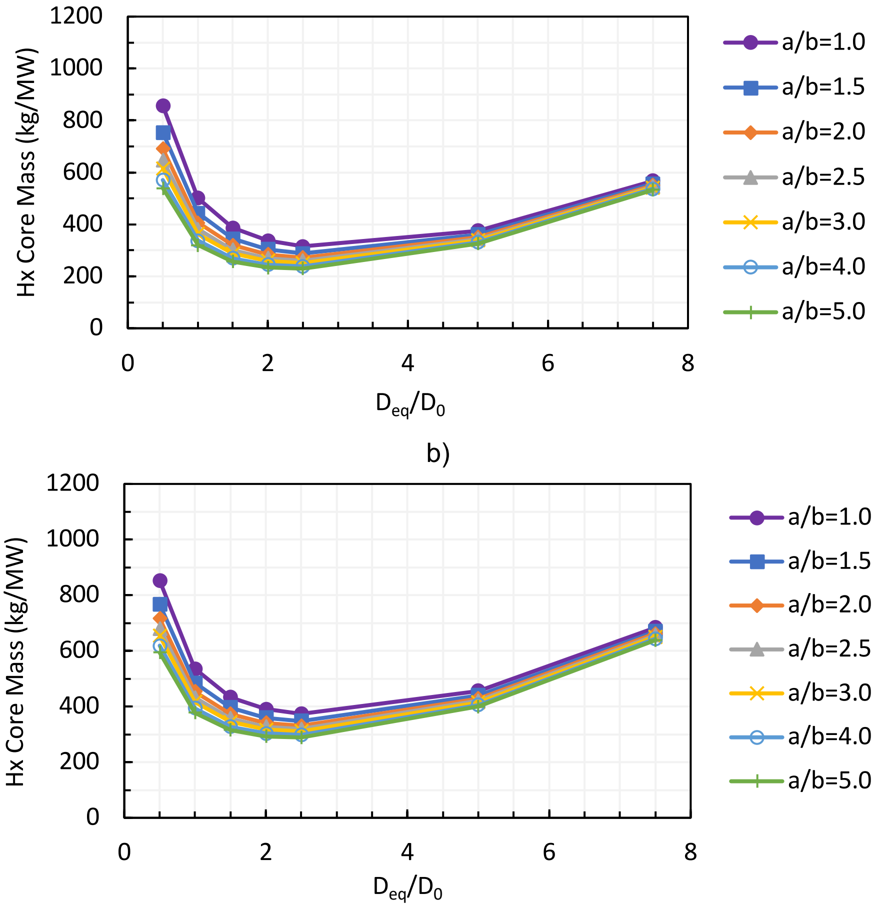

b)

c)

FIGURE 7. Calculated core mass for full factorial experiment cases on PPF geometric parameters with L_{avg} = 0.35 mm: (a) H = 1 mm, (b) H = 2 mm, (c) H = 3 mm.

Aside from the ability to transfer heat at the required rate and the mass of the heat exchanger, the other important factor to consider is the pressure loss. Pressure loss manifests itself economically through pumping costs. A global minimum mass heat exchanger could potentially possess a pressure loss too high for the design to be economical. When considered collectively, the many geometric variations of heat exchangers will span a continuum of performance from high-mass/low pressure drop designs to those that have low-mass and high-pressure loss. The designer's goal is to select designs with a small size and a pressure loss less than some critical value. With these considerations in mind, the specific mass of the PPF design combinations included in the factorial experiment are plotted against the calculated hot-side pressure loss in Figure 8. A maximum pressure drop on the hot fluid side of the PPF heat exchange is set at 0.13 MPa which is consistent with prior work of Jiang et al. [10,11].

The factorial experiment data points show that the smaller pin designs tended to have lower specific mass than the larger pin designs. Although the smaller pin PPF designs had smaller specific mass for a given pressure drop, they are also considered to be less practical from AM perspective, so subsequent discussion will be limited to the 0.35 mm pin designs.

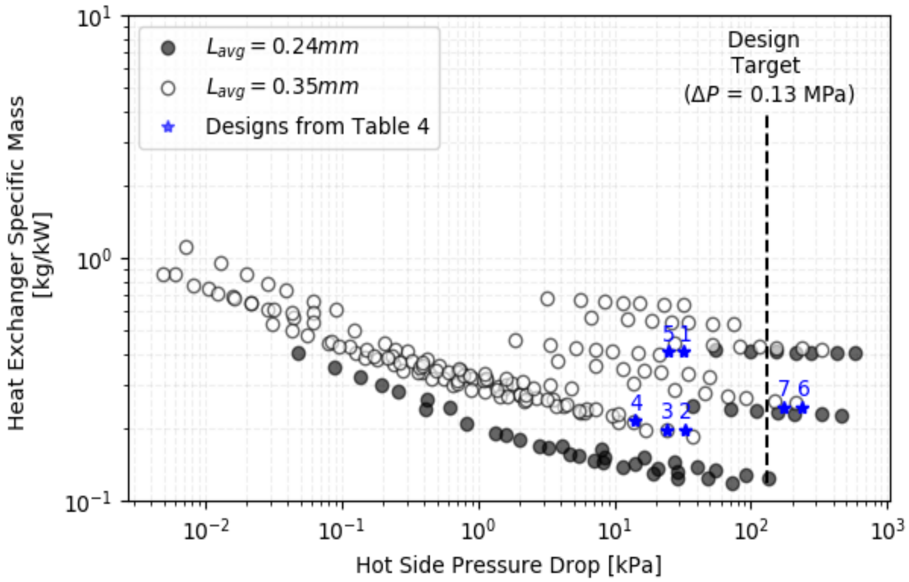

FIGURE 8. Calculated specific mass and pressure drop for the PPF heat exchanger geometries in the factorial experiment (Q_{tot} = 5 kW, constant total hot mass flow rate).

Certain test points from the factorial design were hand-selected for further detailed inspection. These test points are labeled 1-7 on Figure 8. Designs 2, 3, and 4 were selected near the minimum calculated mass for the larger pin size (0.35 mm). After selection, these geometries were rerun in the model, rounding the number of cells up to the next larger even number to avoid fractional cells. In doing so, the pressure loss decreased while the specific mass increased slightly, moving the data points to the left and up in Figure 8, and increasing their heat transfer rate above 5 kW. The data points labeled “6” and “7” were treated differently. In these two cases the fractional number of cells was rounded down, giving them slightly less than 5kW. Designs 1 and 5 were selected because they have a pressure drop similar to Designs 2 and 3, but a mass that is much closer to that of a 5kW printed circuit heat exchanger. The geometric parameters for these seven data points are listed in Table 3. Note that these designs tend to be those with the larger diameters and longer aspect ratios. Design “4” is highlighted in bold-font as it is the design most likely to fit on a typical LPBFAM build platform.

Figure 9 shows several different heat exchanger designs for a much larger (~45 MW) application, but operating at similar pressure, temperature, and overall heat exchanger effectiveness (see Table 4). Based on these data from Jiang et al. [10,11], the CSTEa and CSTEb had the highest specific mass, and the microtube shell and tube heat exchanger (MSTE) had the lowest specific mass. The printed circuit heat exchanger (PCHE) is considered the best commercial offering for a large-scale RCBC recuperator design and the calculated mass for this 45 MW design was between a conventional shell and tube design, and a micro-tube shell and tube design [11,34].

Table 3. Design details for selected PPF heat exchanger geometries (nominally 5 kW and 97% effectiveness)

Design #	Core Mass (kg)	D_{eq}/D0	Cell Major Diam. (mm)	Cell Minor Diam. (mm)	No. Cells	Core Length (mm)	L_{min} (mm)	L_{maj} (mm)	H_{pin} (mm)	S_T-L_{min} (mm)	Plate Thickness (mm)
1	2.09	5	495	165	4	7	0.3	0.415	1	0.3	0.6
2	0.99	2.5	320	64	8	13.4	0.3	0.415	1	0.3	0.6
3	0.98	2.5	286	71.5	8	13.4	0.3	0.415	1	0.3	0.6
4	**1.08**	**2**	**256**	**51.2**	**14**	**23**	**0.3**	**0.415**	**1**	**0.3**	**0.6**
5	2.09	5	452	181	4	7	0.3	0.415	1	0.3	0.6
6	1.21	5	640	128	2	3.8	0.3	0.415	1	0.3	0.6
7	1.21	5	572	143	2	3.8	0.3	0.415	1	0.3	0.6

Table 4. Comparison of PPF HX designs with other reference HXs [11]

Point Designation	HX Designation	Q (kW)	Pressure Drop (kPa)	Mass (kg)	M/Q (kg/kW)
4	PPF	5.01	14	1.08	0.216
5	PPF	5.08	24	2.09	0.411
7	PPF	4.97	172	1.21	0.243
A [11]	CSTEa	45,150	130	52,770	1.169
B [11]	CSTEb	45,150	130	24,020	0.532
C [11]	MSTE	45,150	130	5,090	0.113
D [11]	PCHE	45,150	130	11,400	0.252
2 plates	PCHE	5.0	113	1.87	0.374
20 plates	PCHE	5.0	5.8	4.75	0.950
50 plates	PCHE	5.0	0.1	17.8	3.560

The pressure drop and specific mass for the PCHE described in Jiang et al. [10,11] is comparable to the PPF designs in Table 3, but the size and heat duty for these two applications are significantly different. In order to make a better comparison at a similar scale, the model developed by Jiang et al. [10,11], was used to estimate the size and pressure drop for a printed circuit heat exchanger with a 5kW heat duty. These results are shown as square data points in Figure 9. The PPF designs listed in Table 3 have a lower pressure drop or a lower specific mass than the 5 kW PCHE predictions. Although numerous issues still exist for deployment of larger scale additively manufactured heat exchanger concepts like the PPF, the potential to achieve similar performance as a printed circuit heat exchanger at small scales seems plausible.

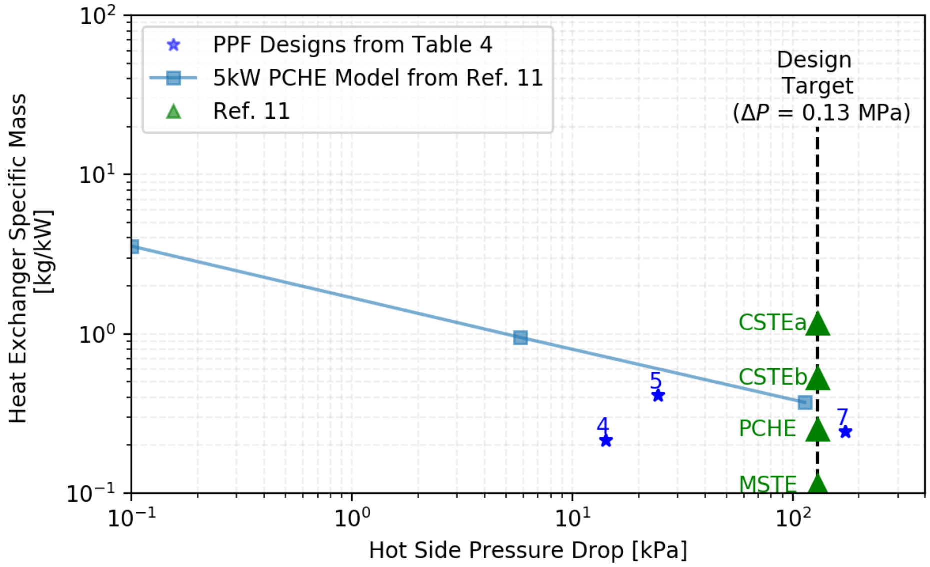

FIGURE 9. Pressure drop and specific mass for PPF heat exchanger designs from Table 4 and other heat exchanger concepts described previously.

3.3.3 Steepest Descent Optimization

A PPF heat exchanger design can be found to accommodate nearly any specific heat duty by varying the geometric parameters and number of cells. A very large number of design variations exist for a 5kW PPF heat exchanger. However, not all these designs may be practical from the perspectives of material expense, physical size, pressure loss, and manufacturing considerations (e.g., can be at least fabricated by AM). The PPF model was used to identify

5kW designs that can be fabricated and comparable with other heat exchanger designs with respect to the specific mass and pressure loss characteristics. A steepest descent optimization method [35] was applied to minimize the 5 kW PPF heat exchanger mass, as the mass is an important factor in the overall cost of a heat exchanger.

The 1D PPF heat exchanger model was used to estimate its thermohydraulic performance. Initial parameter values and constraints are shown in Table 5. The heat duty was fixed at 5kW. The number of cells was calculated for each design to maintain this heat duty. The dimensionality of the problem was further reduced by fixing three geometric parameters (L_{wall}, L_{maj}/L_{min}, and S_LS_T) to constant values. Other parameters were restricted to fall within specified ranges. Most of these ranges were established due to limitations imposed by the capabilities of LPBFAM (e.g., D_{eq} and (a/b)), which were estimated so that the heat exchanger would fit on the build volume. L_{min} and S_T-L_{min} limits were set in accordance with the minimum feature size that the LPBFAM was capable of resolving. The metal used in fabrication of the heat exchanger was assumed to be 316L stainless steel with a density of 8,440 kg/m^3.

Table 5. Parameters & values for steepest descent optimization

Parameter #	Parameter	Units	Initial Value	Minimum	Maximum	Other Restrictions
-	Q	kW	5	5	5	Q=5 kW
-	N	cells	2194	n/a	n/a	Q(N)=5 kW
1	D_{eq}	m	0.0572	0.040	0.254	
2	(a/b)	-	1	1	5	
3	Y_f/a	-	0.5569	0.25	0.75	
4	H_{pin}	m	0.003	0.001	0.003	
5	L_{min}	m	0.0013	0.0003	0.003	
6	S_T-L_{min}	m	0.0007	0.0003	0.003	
-	L_{wall}	m	0.0006	0.0006	0.0006	$L_{wall} = 0.006\, m$
-	L_{maj}/L_{min}	-	1.3846	1.3846	1.3846	$\frac{L_{maj}}{L_{min}} = 1.3846$
-	S_L/S_T	-	0.75	0.75	0.75	S_L/S_T=0.75

Due to the wide magnitude ranges of the dependent variables, dimensionless variables were considered, i.e., $x_i = (X_i - X_{i,min})/(X_{i,max}-X_{i,min})$ where lower case x_i represents the ith dimensionless variable, X_i represents the original variable, and $X_{i,min}$ and $X_{i,max}$ are its minimum and maximum values as listed in Table 5. Thus, the mass of a specific 5 kW PPF design becomes a function of six dimensionless variables, e.g. $M(x)=F(x_1, x_2, x_3, x_4, x_5, x_6)$. The "mass" gradient with respect to x, which is calculated as $G(x)=dM(x)/dx = (dF/dx_1, dF/dx_2, dF/dx_3, dF/dx_4, dF/dx_5, dF/dx_6)$ is a vector that "points" in the "up-slope" direction. If $M(x^0)$ is the mass of the initial design, then $M(x^1) = M(x^0 - \lambda G(x^0))$ should be less than $M(x^0)$ provided that λ is small enough. The minimization procedure starts with an initial design point x^0 and proceeds iteratively, updating the design based on the gradient until the gradient is "near" zero at a local minimum or x is constrained by other limits. In this exercise, the gradient derivatives were computed numerically using the 1D PPF model. The step size λ was set $\lambda = \frac{0.01}{\mathrm{sqrt}(G(x^n)'G(x^n))}$ so that "small" steps were taken when the gradient was large and larger steps were taken when the gradient was small.

The steepest descent method to minimize a multivariable function was used for its simplicity and ease of programming. Preliminary results indicated that this technique was adequate to demonstrate the capabilities of the PPF design. The initial 5kW PPF heat exchanger contained 2194 flow cells and had a core mass of approximately 66.3 kg. The most sensitive parameter in the early stages was S_T-L_{min}, which converged towards its restricted minimum of 0.3 mm in 20 iterations while the mass decreased to about 13 kg (see Figure 10). After S_T-L_{min} reached its minimum limit, the process continued until L_{min}. reached its minimum constraint after 56 iterations when the PPF mass was reduced to 2.7 kg. While L_{min} and S_T-L_{min} were locked at their minimum values, D_{eq} and (a/b) continued to grow while Y_f/a continued to reduce through successive iterations. The next parameter to encounter a limit was Y_f/a, which reached its minimum limit 0.25 at iteration number 126 and mass = 1.4 kg.

Continuing the iterations towards a minimum mass 5 kW PPF, D_{eq} and (a/b) continued to grow while H_{pin} decreased. The next significant events occurred when H_{pin} reached an imposed minimum length of 1 mm near iteration number 212 (mass= 0.95 kg) and (a/b) reached an upper limit of 5 near iteration number 228 (mass = 0.92 kg). With all other parameters at constrained limits, D_{eq} continued to grow until a (local) minima was reached. For a D_{eq} value of 0.154 m, a heat exchanger mass of 0.919 kg and 6 flow cells was calculated at iteration number 246. The optimized design along with some of its performance metrics such as fin effectiveness, fin (or pin) efficiency, and the overall effectiveness of the heat exchanger are presented in Table 6.

With the limitations we imposed, the minimization process reduced the specific mass down to 0.919 kg / 5 kw = 0.18 kg/kW while maintaining the pressure loss under 2%. The minimum located here could potentially be "local" minima and the potential for further improvements remains if the fixed parameters were permitted to participate in the optimization. Our goal, however, was not to find the ultimate performance limit but merely to show that the PPF design can be compatible with other heat exchanger designs in terms of specific mass and pressure loss.

The optimal HX architecture has relatively small number of flow cells and it is expected that the flow rate non-uniformity would be small as well. A conceptual analysis was carried out to understand the impact of flow non-uniformity on the thermal performance or the average heat transfer coefficient of the HX. To explain the results, let us consider a simple 2 flow cell PPF HX design. When the mass flow rate in one flow cell was reduced by as much as 20% (mass flow rate in the other cell would increase by 20% to keep the same overall mass flow rate), it resulted in -0.71% decrease in the average heat transfer coefficient. This analysis can be extended for a PPF HX design with six flow cells and would still produce negligible difference in the overall thermal performance.

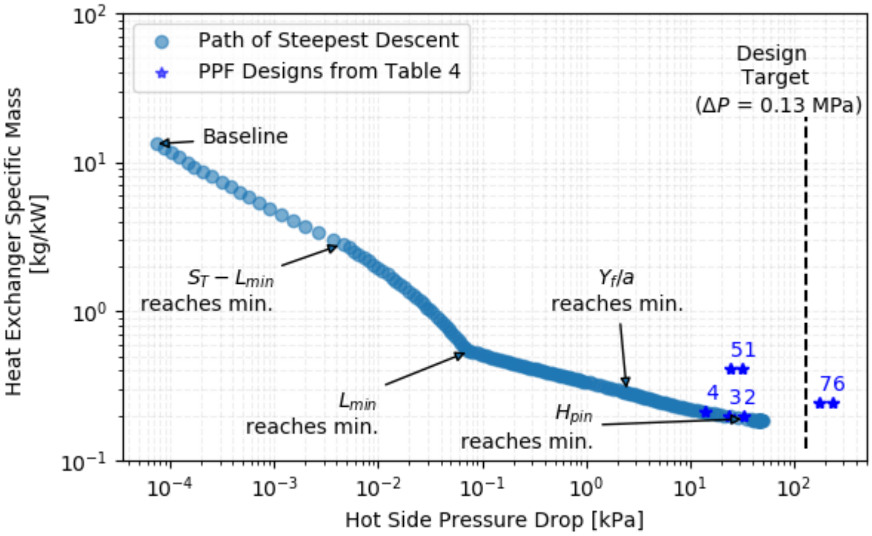

FIGURE 10. Pressure drop and specific mass for PPF heat exchanger designs showing the optimization path of steepest descent compared to PPF designs from Table 3.

Table 6: Optimized Design

Parameter #	Parameter	Units	Optimal Values
-	Q	kW	5
-	N	cells	6
1	D_{eq}	m	0.154 m
2	(a/b)	-	5
3	Y_f/a	-	0.25
4	H_{pin}	m	0.001
5	L_{min}	m	0.0003
6	S_T-L_{min}	m	0.0003
-	L_{wall}	m	0.0006
-	L_{maj}/L_{min}	-	1.3846
-	S_L/S_T	-	0.75
	Fin/Pin Effectiveness		6.8546
	Fin/Pin Efficiency		69.6%: pins on hot side 68.5%: pins on cold side
	Overall HX Effectiveness		97.4%

4.0 CONCLUSIONS

A PPF conceptual design for a novel PPF heat exchanger has been described and optimized using a 1D heat transfer model. The conditions of the inlet streams for this heat exchanger analysis have been chosen to reflect the conditions for a high temperature recuperator in an indirect sCO_2 power cycle. The proposed PPF concept was developed based on a careful consideration of all the heat exchangers for RCBC that were reviewed. The design space investigated in this paper is enabled by AM and some of the design parameters have been constrained based on the knowledge of current AM feature resolutions. An algebraic model of the thermohydraulics of the heat exchanger has been formulated using correlations that are adapted to the proposed geometry.

A 5kW scale device was chosen as a prototype for potential follow-on testing that will help validate the performance predicted by the engineering model described in this paper. To assure that the algebraic model accurately represented this complicated heat exchanger geometry, a CFD model has been used. The CFD model predictions matched the algebraic model heat transfer and pressure drops to within 5%.

A steepest descent method was used to minimize heat exchanger mass for a 5-kW prototype recuperator subject to a maximum specified pressure drop. The optimized solutions resulted in a design with the minimum allowable pin transverse spacing, minimum pin width, minimum pin height and near maximum cell aspect ratio.

Table 4 lists the approximate mass and heat duties for these and other potential recuperator designs. This paper has described a 5 kW PPF concept (i.e., Design #4 in Table 3) that has a low material requirement of 0.216 kg/kW and a pressure drop that is about five times lower than the allowable pressure drop design target.

Although numerous issues still exist for deployment of large-scale additively manufactured heat exchanger concepts, the potential to achieve similar performance at smaller scales could enable new areas for flexible, efficient RCBC sCO_2 power cycles.

ACKNOWLEDGEMENTS

This work was performed in support of the U.S. Department of Energy's Fossil Energy Crosscutting Technology Research Program. The effort at UT-Battelle, LLC, was conducted under Contract No. DE-AC05-00OR22725 with the U.S. Department of Energy for the project "Novel Recuperator Concepts for Supercritical CO_2 based on Additive Manufacturing," and has been funded by the DOE Office of Energy Efficiency and Renewable Energy, Office of Fossil Energy. The authors would also like to thank Keith Carver and Fred List III of ORNL for providing the size limits for AM fabrication.

DISCLAIMER

REFERENCES

[1] Ahn, Y., Bae, S. J., Kim, M., Cho, S. K., Baik, S., Lee, J. I., and Cha, J. E., 2015, "Review of Supercritical CO2 Power Cycle Technology and Current Status of Research and Development," Nucl. Eng. Technol., **47**(6), pp. 647–661.

[2] Garg, P., Kumar, P., and Srinivasan, K., 2013, "Supercritical Carbon Dioxide Brayton Cycle for Concentrated Solar Power," J. Supercrit. Fluids, **76**, pp. 54–60.

[3] Dostal, V., Driscoll, M. J., and Hejzlar, P., 2004, "A Supercritical Carbon Dioxide Cycle for next Generation Nuclear Reactors."

[4] "DOE, 'Energy Department Announces New Investments in Supercritical Transformational Electric Power (STEP) Program,' Department of Energy (DOE)."

[5] Huang, M., Tang, C.-J., and McClung, A., 2018, "Steady State and Transient Modeling for the 10 MWe SCO2 Test Facility Program," *6th International Symposium–Supercritical CO2 Power Cycles*.

[6] Marion, J., Kutin, M., McClung, A., Mortzheim, J., and Ames, R., "The STEP 10 MWe SCO2 Pilot Plant Demonstration," *ASME Turbo Expo 2019: Turbomachinery Technical Conference and Exposition*,

American Society of Mechanical Engineers Digital Collection.

[7] Dyreby, J., Klein, S., Nellis, G., and Reindl, D., 2014, “Design Considerations for Supercritical Carbon Dioxide Brayton Cycles with Recompression,” J. Eng. Gas Turbines Power, **136**(10).

[8] Zitney, S. E., and Liese, E., “Design and Operation of a 10 MWe Supercritical CO2 Recompression Brayton Power Cycle.”

[9] Zada, K. R., Kim, R., Wildberger, A., and Schalansky, C. P., 2018, “Analysis of Supercritical CO2 Brayton Cycle Recuperative Heat Exchanger Size and Capital Cost with Variation of Layout Design,” *Proceedings of the 6th International Supercritical CO2 Power Cycle Symposium, Pittsburgh, PA*.

[10] Jiang, Y., Liese, E., Zitney, S. E., and Bhattacharyya, D., 2018, “Optimal Design of Microtube Recuperators for an Indirect Supercritical Carbon Dioxide Recompression Closed Brayton Cycle,” Appl. Energy, **216**, pp. 634–648.

[11] Jiang, Y., Liese, E., Zitney, S. E., and Bhattacharyya, D., 2018, “Design and Dynamic Modeling of Printed Circuit Heat Exchangers for Supercritical Carbon Dioxide Brayton Power Cycles,” Appl. Energy, **231**, pp. 1019–1032.

[12] Kruizenga, A. M., Fleming, D. D., Carlson, M. D., and Anstey, M., 2014, *Supercritical CO2 Heat Exchanger Fouling.*, Sandia National Lab.(SNL-CA), Livermore, CA (United States); Sandia National ….

[13] Le Pierres, R., Southall, D., and Osborne, S., 2011, “Impact of Mechanical Design Issues on Printed Circuit Heat Exchangers,” *Proceedings of SCO2 Power Cycle Symposium*, University of Colorado Bolder, pp. 24–25.

[14] Sabau, A. S., Shingledecker, J. P., Kung, S. C., Wright, I. G., and Nash, J., 2016, *Exfoliation Propensity of Oxide Scale in Heat Exchangers Used for Supercritical CO2 Power Cycles*, Oak Ridge National Lab.(ORNL), Oak Ridge, TN (United States).

[15] Kung, S. C., Shingledecker, J. P., Thimsen, D., Wright, I. G., Tossey, B. M., and Sabau, A. S., 2016, “Oxidation/Corrosion in Materials for Supercritical CO2 Power Cycles,” *Proceedings of the 5th International Symposium on Supercritical CO2 Power Cycles, San Antonio, TX.*

[16] Webb, R. L., 1981, “Performance Evaluation Criteria for Use of Enhanced Heat Transfer Surfaces in Heat Exchanger Design,” Int. J. Heat Mass Transf., **24**(4), pp. 715–726.

[17] Black, J., Straub, D., Robey, E., Yip, J., Ramesh, S., Roy, A., and Searle, M., 2020, “Measurement of Convective Heat Transfer Coefficients With Supercritical CO2 Using the Wilson-Plot Technique,” J. Energy Resour. Technol., **142**(7).

[18] Musgrove, G., Sullivan, S., Shiferaw, D., Fourspring, P., and Chordia, L., 2017, “8 - Heat Exchangers,” K. Brun, P. Friedman, and R.B.T.-F. and A. of S.C.D. (sCO$_2$) B.P.C. Dennis, eds., Woodhead Publishing, pp. 217–244.

[19] Sabau, A. S., Bejan, A., D., B., Gluesenkamp, K. R., Murphy, B. L., F.A., L.-I., K., C., Schaich C.R., A., and J.W., K., 2020, *Design, Additive Manufacturing, and Performance of Heat Exchanger with a Novel Flow-Path Architecture*.

[20] Kind, M., Martin, H., Stephan, P., Roetzel, W., Spang, B., Müller-Steinhagen, H., Luo, X., Kleiber, M., Joh, R., and Wagner, W., 2010, “VDI Heat Atlas.”

[21] Gnielinski, V., 2010, *VDI Heat Atlas*, Springer Berlin Heidelberg, Berlin, Heidelberg.

[22] Kreith, F., and Bohn, M. S., 1997, “Principles of Heat Transfer 5th Edition,” A59.

[23] Wright, A. D., and Heggs, P. J., 2002, “Rating Calculation for Plate Heat Exchanger Effectiveness and Pressure Drop Using Existing Performance Data,” Chem. Eng. Res. Des., **80**(3), pp. 309–312.

[24] Bergman, T. L., Incropera, F. P., DeWitt, D. P., and Lavine, A. S., 2011, *Fundamentals of Heat and Mass Transfer*, John Wiley & Sons.

[25] Li, W., Ren, J., Hongde, J., Luan, Y., and Ligrani, P., 2015, “Assessment of Six Turbulence Models for Modeling and Predicting Narrow Passage Flows, Part 2: Pin Fin Arrays,” Numer. Heat Transf. Part A Appl., (November).

[26] Gnielinski, V., 2010, “G7 Heat Transfer in Cross-Flow around Single Rows of Tubes and through Tube Bundles,” *VDI Heat Atlas*.

[27] Incropera, 2007, *Fundamentals of Heat and Mass Transfer*.

[28] Metzger, D. E., Shepard, W. B., and Haley, S. W., 1986, “Row Resolved Heat Transfer Variations in Pin-Fin Arrays Including Effects of Non-Uniform Arrays and Flow Convergence,” *Turbo Expo: Power for Land, Sea, and Air*, American Society of Mechanical Engineers, p. V004T09A015.

[29] Chyu, M. K., Hsing, Y. C., Shih, T.-P. I.-P., and Natarajan, V., 1999, “Heat Transfer Contributions of Pins and Endwall in Pin-Fin Arrays: Effects of Thermal Boundary Condition Modeling,” J. Turbomach., **121**(2), pp. 257–263.

[30] Žukauskas, A., 1972, “Heat Transfer from Tubes in Crossflow,” *Advances in Heat Transfer*, Elsevier, pp. 93–160.

[31] “NETL. Recuperator Technology Development and Assessment for Supercritical Carbon Dioxide (SCO2) Based Power Cycles. Funding Opportunity Number: DE-FOA- 0001239; March 2015.”

[32] White, C. W., Shelton, W., Weiland, N., Shultz, T., Plunkett, J., and Gray, D., 2017, *Techno-Economic Evaluation of Utility-Scale Power Plants Based on the Indirect SCO2 Brayton Cycle-Report*, NETL.

[33] Searle, M., Black, J., Straub, D., Robey, E., Yip, J., Ramesh, S., Roy, A., Sabau, A. S., and Mollot, D., 2020, “Heat Transfer Coefficients of Additively Manufactured Tubes with Internal Pin Fins for Supercritical Carbon Dioxide Cycle Recuperators,” Appl. Therm. Eng., **181**, p. 116030.

[34] Marchionni, M., Chai, L., Bianchi, G., and Tassou, S. A., 2019, “Numerical Modelling and Transient Analysis of a Printed Circuit Heat Exchanger Used as Recuperator for Supercritical CO2 Heat to Power Conversion Systems,” Appl. Therm. Eng., **161**(July), p. 114190.

[35] Cheney, W., and Kincaid, D., 1985, “Numerical Mathematics and Computing, Brooks,” Cole Pub.

[36] Lemmon, E. W., Bell, I. H., Huber, M. L., and McLinden, M. O., 2018, “NIST Standard Reference Database 23: Reference Fluid Thermodynamic and Transport Properties-REFPROP, Version 10.0, National Institute of Standards and Technology.”

[37] Span, R., and Wagner, W., 1996, “A New Equation of State for Carbon Dioxide Covering the Fluid Region from the Triple-Point Temperature to 1100 K at Pressures up to 800 MPa,” J. Phys. Chem. Ref. Data, **25**(6), pp. 1509–1596.

Appendix I

1-D MODEL

The total resistance to heat transfer from the hot to the cold fluid is $R_{tot} = R_{hot} + R_{cond} + R_{cold}$. The total thermal conductance from the hot cells is $\frac{1}{R_{hot}} = \sum h_{pri} A_{primary.pop} + \sum h_{pin} \epsilon_{pin} A_{pin}$. The primary area per hot cell is the heat exchange area of the plate walls separating the cell from its cold-flow neighbors, less the surface area obstructed by the pin fins:

$$A_{primary.pop} = \begin{cases} 2 * A_{populated} - \frac{A_{populated}}{S_T^2 \left({S_L}/{S_T} \right)} L_{avg}^2 & for\ two - sided\ cells \\ A_{populated} - 0.5 \frac{A_{populated}}{S_T^2 \left({S_L}/{S_T} \right)} L_{avg}^2 & for\ one - sided\ cells \end{cases} \tag{4}$$

The heat transfer coefficient for the primary surface was estimated via the standard Dittus-Boelter correlation [22] for the Nusselt number:

$$h_{pri} = \frac{Nu_{pri} \cdot k_{gas}}{D_{h.pop}} \tag{5}$$

$$Nu_{pri} = 0.023 {Re_{pri}}^{0.8} Pr^{0.3} \tag{6}$$

and,

$$Re_{pri} = \frac{\left(\frac{\dot{m}}{A_{xs.avg.pop}} \right) D_{h.pop}}{\mu_{gas}} \tag{7}$$

where k_{gas} is the thermal conductivity of the supercritical CO_2, $D_{h.pop}$ is the hydraulic diameter of the elliptical flow cell (in the populated zone only), Pr is the Prandtl number of the sCO_2, $\dot{m}$ is the mass flow of sCO_2 per cell, $A_{xs.avg.pop}$ is the average cross-sectional void area in the pin field, perpendicular to the primary axis, and μ_{gas} is the dynamic viscosity of the sCO_2. The gas properties for the cold and hot fluid streams were computed via Refprop [36,37] at their respective inlet pressures and using the average of their inlet and estimated outlet temperatures.

The heat exchange rate for the pins is governed by the number of pins per cell, surface area per pin, the pin efficiency, and the pin heat transfer coefficient. The pin area per cell is given by

$$A_{pin} = \frac{A_{populated}}{S_T^2 \left({S_L}/{S_T} \right)} \cdot \left(2 L_{avg} \sqrt{\gamma_p + {1}/{\gamma_p}} \right) \cdot H_{pin} \tag{8}$$

while the pin efficiency is calculated as

$$\epsilon_{pin} = k_{metal} \frac{L_{avg}^2}{2} m_c \frac{\tanh \left(m_c H_{pin} \right)}{h_{pin} \left(2 L_{avg} \sqrt{\gamma_p + {1}/{\gamma_p}} \right) H_{pin}} \tag{9}$$

where k_{metal} is the thermal conductivity of the metal, h_{pin} is the pin heat transfer coefficient (defined later) and

$$m_c = \sqrt{\frac{h_{pin} \left(2 L_{avg} \sqrt{\gamma_p + {1}/{\gamma_p}} \right)}{k_{metal} \frac{L_{avg}^2}{2}}}. \tag{10}$$

In order to compute the heat transfer coefficient for the pin fins, one must first consider the effect of pin size and spacing on the mass flux through the pin field. Let $A_{xs.avg.free}$, as shown in the equation below, represent the average cross-sectional area (perpendicular to flow) in the pin zone in the absence of pins.

$$A_{xs.avg.free} = \frac{A_{populated} \cdot H_{pin}}{2 \left(a - Y_f \right)} \tag{11}$$

The mass flux relative to this area will be accelerated by a factor of γ_{max} that depends on the gap between adjacent pins on the same row, or the gap between pins on alternate rows, whichever is more restrictive.

$$d_T = S_T \left(1 - \left(\frac{L_{avg}}{S_T \sqrt{\gamma_{pin}}} \right) \right) \tag{12}$$

$$d_{L'} = S_T \left(\frac{1}{2} + \frac{1}{\gamma_{pin}} \left({S_L}/{S_T} \right) - \frac{L_{avg}}{S_T \sqrt{\gamma_{pin}}} \right) \frac{\gamma_{pin}}{\sqrt{\gamma_{pin}^2 + 1}} \tag{13}$$

$$\gamma_{max} = \begin{cases} \dfrac{S_T/2}{d_{L'}} & 2d_{L'} \le d_T \\ \dfrac{S_T}{d_T} & otherwise \end{cases} \tag{14}$$

However, in the applied version of the PPF model, the diamond-shaped pins were approximated by cylindrical pins with an equivalent diameter of $D_{eq} = L_{avg}\sqrt{2/\pi}$. In this case,

$$d_T = S_T\left(1 - \sqrt{2/\pi}\left(\frac{L_{avg}}{S_T}\right)\right) \tag{15}$$

$$d_{L'} = S_T\left(\sqrt{\frac{1}{4} + \left(S_L/S_T\right)^2} - \sqrt{2/\pi}\left(\frac{L_{avg}}{S_T}\right)\right) \tag{16}$$

$$\gamma_{max} = \begin{cases} \dfrac{S_T/2}{d_{L'}} & 2d_{L'} \le d_T \\ \dfrac{S_T}{d_T} & otherwise \end{cases} \tag{17}$$

After γ_{max} is found, the maximum mass flux is

$$\left(\frac{\dot{m}}{A}\right)_{pin.max} = \gamma_{max}\frac{\dot{m}}{A_{xs.avg.free}} \tag{18}$$

and the Reynolds number proceeds as "normal":

$$Re_{pin} = \frac{\left(\frac{\dot{m}}{A}\right)_{pin.max} L_{min}}{\mu_{gas}} \tag{19}$$

The pin width was chosen as the characteristic length. The Nusselt number for the pins was estimated by combining Nusselt number correlations for pins in laminar and turbulent flows [20,21,26]:

$$Nu_{lam} = 0.664 \cdot {Re_{pin}}^{0.5} Pr^{0.333} \tag{20}$$

$$Nu_{turb} = \frac{0.037 \cdot {Re_{pin}}^{0.8} Pr}{1 + 2.443 \cdot {Re_{pin}}^{-0.1}\left(Pr^{0.667} - 1\right)} \tag{21}$$

$$Nu_{pin} = 0.3 + \sqrt{Nu_{lam}^2 + Nu_{turb}^2} \tag{22}$$

The heat transfer coefficient for the pin surfaces was calculated from this combined Nusselt number:

$$h_{pin} = \frac{Nu_{pin} \cdot k_{gas}}{L_{min}} \tag{23}$$

Likewise, the total thermal conductance to the cold fluid is

$$\frac{1}{R_{cold}} = \sum h_{pri} A_{primary.pop} + \sum h_{pin} \gamma_{pin} A_{pin} \tag{24}$$

Calculation of the heat transfer coefficients, heat transfer areas, and pin efficiencies for the cold surfaces was nearly identical to that for the hot surfaces, except for the Dittus-Boelter exponent used to calculate the Prandtl number (0.4 for the hot surfaces, 0.3 for the cold surfaces).

Resistance to heat flow through the cell walls is approximated by

$$\frac{1}{R_{cond}} = \frac{k_{metal} A_{cond.tot}}{L_{wall}} \tag{25}$$

where

$$A_{cond.tot} = (N_{cells} - 1)\frac{\pi D^2}{4}\left(\frac{A_{pop}}{A_{disk}}\right) \tag{26}$$

Given the tally of all the thermal resistances, the number of thermal units is given by

$$NTU = \frac{{}^{1}/_{R_{tot}}}{minimum(\dot{m}_{cold}c_{p.cold}, \dot{m}_{hot}c_{p.hot})} \tag{27}$$

For counter-flow heat exchangers, this NTU corresponds to a heat exchanger effectiveness of

$$\epsilon = \frac{1-e^{-(NTU)(1-c_R)}}{1-c_R e^{-(NTU)(1-c_R)}} \tag{28}$$

where

$$c_R = \frac{minimum(\dot{m}_{cold}c_{p.cold}, \dot{m}_{hot}c_{p.hot})}{maximum(\dot{m}_{cold}c_{p.cold}, \dot{m}_{hot}c_{p.hot})} \tag{29}$$

Given the effectiveness, we can solve for the rate of heat transfer within the PPF:

$$Q = \epsilon \cdot minimum(\dot{m}_{cold}C_{p.cold}, \dot{m}_{hot}C_{p.hot}) \cdot (T_{in.hot} - T_{in.cold}) \tag{30}$$

The pressure losses incurred by the hot and cold streams as they flow through the heat exchanger are also of interest. The pressure loss was assumed to be largely due to the loss across the pin field, which was treated similar to a tube bank. The pressure loss correlation applied in this model is

$$\Delta P = f \cdot N_{rows} \cdot 1.1\frac{\rho_{gas}}{2}V_{max}{}^2 \tag{31}$$

where the friction factor f ([22]) was estimated as

$$f = 0.4799 - 0.00001045 \cdot Re_{max} + \frac{84.9217}{Re_{max}} \tag{32}$$

and the Reynolds number is the same as that used for calculation of the pin field heat transfer coefficient [21] and the velocity was computed from the pin-field mass flux:

$$V_{max} = \frac{\left(\frac{\dot{m}}{A}\right)_{pin.max}}{\rho_{gas}} \tag{33}$$